Observation of supersymmetric pseudo-Landau levels
in strained microwave graphene

Matthieu Bellec*,[1] Charles Poli,[2] Ulrich Kuhl,[1]

Fabrice Mortessagne*,[1] and Henning Schomerus*[2]

[1]*Université Côte d'Azur, CNRS, Institut de Physique de Nice (INPHYNI), 06108 Nice, France*

[2]*Department of Physics, Lancaster University, Lancaster, LA1 4YB, United Kingdom*

*matthieu.bellec@inphyni.cnrs.fr, Fabrice.Mortessagne@unice.fr, h.schomerus@lancaster.ac.uk

Using an array of coupled microwave resonators arranged in a deformed honeycomb lattice, we experimentally observe the formation of pseudo-Landau levels in the whole crossover from vanishing to large pseudomagnetic field strength. This is achieved by utilizing an adaptable set-up in a geometry that is compatible with the pseudo-Landau levels at all field strengths. The adopted approach enables us to observe fully formed flat-band pseudo-Landau levels spectrally as sharp peaks in the photonic density of states, and image the associated wavefunctions spatially, where we provide clear evidence for a characteristic nodal structure reflecting the previously elusive supersymmetry in the underlying low-energy theory. In particular, we resolve the full sublattice polarization of the anomalous 0th pseudo-Landau level, which reveals a deep connection to zigzag edge states in the unstrained case.

Introduction

Topological states enjoy intense attention as they equip quantum systems with desirable robust properties. Much of the early focus rested on their unique spectral positions as isolated or dispersive states in a band gap, as well as their spatial localization at edges and interfaces[1], or more recently also corners[2]. More fundamental characterizations, on the other hand, often invoke a third, somewhat deeper feature of topological states, which is connected to the anomalous expectation values of the underlying symmetry operators[3,4]. In momentum space, this feature underpins, e.g., the unidirectional chiral currents around the edges of topological insulators, whilst in real space it manifests itself, e.g., in the sublattice polarization of defect states in bipartite lattice systems[5], as has been exploited in recent topological lasers or non-linear limiters based on photonic Su-

32   Schrieffer-Heeger structures[6-9].

34   An additional attractive aspect of these anomalous features are that they tie topological effects
35   together that are often seen as separate, due to the varied nature of the specific encountered spectral
36   and spatial features that first come into focus. A prime example are flat bands, which have been
37   observed in recent experiments focussing on Lieb lattices[10-13] and one-dimensional counterparts[14],
38   as well as suitably deformed graphene[15] and analogous quantum[16] and classical systems[17,18]. In the
39   latter case they constitute pseudo-Landau levels arising from a synthetic magnetic field[19]. In
40   particular, signatures of photonic pseudo-Landau levels have been detected by probing the edges
41   of a honeycomb array of optical waveguides[17]. A second example are a class of helical edge states
42   in reciprocal systems, as observed, e.g., in zigzag terminated graphene[20,21]. While these bulk and
43   edge phenomena do not naturally fall into the scope of standard topological band structure theory[1],
44   they are still intimately linked to wavefunctions with a characteristic sublattice polarization. This
45   provides a promising perspective from which one can seek to develop very general unifying
46   descriptions (see, e.g., ref. 22 for a recent approach utilizing this perspective).

48   In this work, we demonstrate experimentally for the case of photonic graphene-like systems that
49   the anomalous edge and bulk phenomena tied to sublattice polarization are in fact directly linked.
50   This is achieved by tracing the formation of pseudo-Landau levels all the way from vanishing to
51   large pseudomagnetic field strengths. In particular, we report the direct observation of the spatially
52   resolved sublattice polarization in the 0th pseudo-Landau level of strained photonic graphene, and
53   trace it back to the unstrained case, where the system only possesses edge states. By observing a
54   characteristic nodal structure for the higher-order levels, we can then establish a direct link to the
55   supersymmetric Hamiltonian of the underlying low-energy theory[23]. Thereby, our observations
56   connect a broad variety of topological phenomena to a unifying principle.

58   **Results**

60   **A. Microwave set-up and optimal strain geometry**

62   Our experimental set-up is illustrated in Fig. 1. The unstrained system forms a honeycomb lattice

63   with nearest-neighbor spacing $a_0 = 13.9$ mm, combining two triangular lattices of A and B sites,

64   where each vertex denotes the position of a dielectric microwave resonator with bare frequency

65   $\omega_0 = 6.653$ GHz, while adjacent resonators are coupled at strength $t_0 = 21.5$ MHz (for details

66   see the materials and methods section). This gives rise to a standard graphene-like photonic band

67   structure[24,25], with two Dirac cones at the K and K' points in the Brillouin zone. Around these two

68   so-called valleys, at relative momentum $\boldsymbol{q}$, the low-energy dispersion $\omega(\boldsymbol{q}) \sim \omega_0 \pm v|\boldsymbol{q}|$ resembles

69   massless relativistic particles moving in two dimensions at velocity $v = 3a_0 t_0/2$.

70

71   In the deformed system, the indicated couplings t_l depend on the distances to the three neighboring

72   resonators, which we can utilize to create a pseudomagnetic field corresponding to that in strained

73   graphene. Such a field arises when the resonators are displaced non-uniformly, where the positions

74   are selected to give a triaxial spatial coupling profile[19,26]

75

76
$$t_l = t_0 \left[1 - \frac{\beta}{2a_0^2} \boldsymbol{\rho}_l \cdot \boldsymbol{r} \right], \tag{1}$$

77

78   where $\boldsymbol{r}$ refers to the positions of the links between the coupled resonators in the unstrained system

79   and the bond vectors $\boldsymbol{\rho}_l$ are pointing along these coupling directions. This coupling profile ensures

80   a constant pseudomagnetic field of strength β throughout the whole system. Theoretically, the

81   system is well described in a coupled-mode theory with nearest-neighbour couplings t_l as given

82   above, so that the eigenfrequencies and mode profiles can be obtained from an effective

83   Hamiltonian H. As any such bipartite system, it then displays a chiral symmetry relative to the

84   central frequency, $\Sigma_z (H - \omega_0) \Sigma_z = -(H - \omega_0)$, where the Pauli-like matrix Σ_z acts on the

85   sublattice degree of freedom, hence keeps the amplitudes on A sites fixed but inverts those on the

86   B sites. The balance of zero modes on the A and B sublattices is given by the signature of this

87   operator[13,27],

88

89   #(A zero modes) − #(B zero modes) = tr Σ_z = #(A sites) − #(B sites) .   (2)

90

91   These zero modes have frequency ω_0, and as indicated are localized on a given sublattice.

92   Furthermore, the chiral symmetry dictates that all non-zero modes occur in spectral pairs at

93   symmetric positions $\omega_0 \pm \delta\omega$, and have equal intensity on both sublattices.

94

95   Importantly, and in contrast to earlier experimental work, we select a triangular geometry and

96   terminate the system with zigzag edges. This ensure a number of beneficial features[28,29].

97   Particularly relevant for us, the boundary conditions are then compatible with the bulk pseudo-

98   Landau levels at all field strengths; furthermore, a consistent coupling profile can be maintained

99   even at maximal field strength, whose description requires to go beyond the conventional low-

100 energy analogy to magnetic fields with opposite signs in the two valleys. Setting the

101 pseudomagnetic field strength to a fixed value, we then see that the values of the couplings dictated

102 by the profile (1) drop to zero exactly at the terminating edges of a zigzag terminated triangle. The

103 corresponding maximal field strength is $\beta_M = 4/L$, where the size parameter L counts the

104 terminating A sites along each edge.

105

106 In the experiments we realize these conditions in a system with 196 resonators, corresponding to

107 a triangle with $L = 14$ resonators along each terminating edge (see Fig. 1). Of these, 105

108 resonators are on the A sublattice while 91 are on the B sublattice. This allows us to realize field

109 strength up to $\beta = 0.2$, where the extremal couplings still exceed the homogeneous resonator

110 linewidth $\gamma = 1.7$ MHz, and sufficiently close to β_M to clearly demonstrate the detailed features

111 of well-formed pseudo-Landau levels. To obtain the analogous orbital effects for an electron in

112 graphene, a magnetic field of 42000 T would have to be applied.

113

114   **B. Formation of pseudo-Landau levels**

115

116 Figure 2 shows our main experimental results. The panels on the left show the density of states for

117 the resonator geometry on the right, where each row corresponds to a different value of the

118 pseudomagnetic field strength β. The color density plot overlayed with the resonator lattice depicts

119 the local density of states integrated over the central peak, situated at the bare resonator frequency

120 ω_0.

121

122 In the pristine system ($\beta = 0$), this peak arises from the zigzag edge states, which are localized on

123 the terminating resonators. Note that these resonators all occupy the same sublattice of A sites. On

124 this sublattice, the zigzag states decay into the bulk of the system, whilst they maintain a vanishing
125 density on the B sublattice. The simple rule (2) can be exploited to count the number of these
126 zigzag states: As a consequence of the chiral symmetry of the system, this number is expected as
127 the difference $105 - 91 = 14 = L$ of A and B sites in the system. Away from the central peak,
128 the density of states displays a broad continuum, with fluctuations arising from the finite-size
129 quantization of bulk graphene-like states, including the states near the Dirac cones.

130

131 As the pseudomagnetic field strength is increased, we observe that the spectral weight from this
132 continuum gradually reorganises into a sequence of well-defined peaks, which at large field
133 strength obtain a similar width and weight as the central peak. Furthermore, whilst the weight and
134 position of the central peak itself remains essentially unchanged, the spatial profile of the
135 associated zero-modes changes significantly, in that they move into the bulk, where they form the
136 desired 0th pseudo-Landau level.

137

138 The observed spectral positions of the emerging higher-order pseudo-Landau levels conform well
139 with the characteristic square-root dependence on relativistic Landau levels[23,30], revisited later in
140 the text and depicted by the gray dashed lines in Fig. 2. The same applies to the observed spectral
141 weights. As the transformation from the zigzag edge states to the 0th pseudo-Landau level is
142 continuous, this bulk level retains the same spectral degeneracy, hence here consists of $L = 14$
143 modes. The coupled-mode theory predicts that the nth pseudo-Landau level encompasses $14 -$
144 $|n|$ states, which explains the gradual drop of the observed spectral weights of the peaks moving
145 outwards from the central peak. Note that this implies an important difference to Landau levels
146 arising from a magnetic field, for which the degeneracy is dictated by the sample area $\propto L^2$, but
147 not the linear size L, as observed here and underpinned by general theory[28,29].

148

149

150   **C. Supersymmetric nodal profiles**

151

152 As anticipated, a notable feature in the formation of the 0th pseudo-Landau level verified in the
153 experiment is the observation that across the whole transition, the associated modes remain
154 localized on the A sublattice. In contrast, the modes in the emerging higher-order levels, whilst

155 also localized in the bulk, are anticipated to display an equal weight on both sublattices. We

156 analyze this distinction in detail in Fig. 3. The top rows display the experimental local density of

157 states in the spectral range of the pseudo-Landau levels for the indices $n = 0,1,2,3,4$, all taken at

158 the large pseudomagnetic field strength $\beta = 0.2$. As above, the level with $n = 0$, shown in the left

159 panels, is located on the A sublattice. The higher-order levels shown in the other panels indeed

160 display an approximately equal weight on both sublattices. Furthermore, they have an intensity

161 profile that increasingly seeps into the corner areas of the triangle, which remains in line with the

162 predictions of coupled-mode theory where the states form a complete basis.

163

164 The other two rows in Fig. 3 show the local density of states along the edges of the system

165 separately for the A and B sublattice, where we averaged over the three edges and indicate the

166 range of observed values by the shaded areas. For the higher-order levels, we furthermore include

167 the levels with index $-n$ into the average. Along each edge, we observe standing-wave patterns

168 with a characteristic nodal pattern represented by oscillating functions

169

$$\psi_r^{(A,\,\text{edge})} \propto \sin[(|n| + 1)\pi r/(L + 1)] \tag{3}$$

171

172 for resonator $r = 1,2,3, \ldots, L$ on the A sublattice, and a corresponding pattern

173

$$\psi_r^{(B,\,\text{edge})} \propto \sin(|n|\pi r/L) \tag{4}$$

175

176 for resonator index $r = 1,2,3, \ldots, L - 1$ on the B sublattice.

177 The key observation is that the mode index $(|n| + 1)$ vs $|n|$ in these patterns for the two sublattices

178 is offset by one, which directly translates into the same offset of the number of nodal points along

179 each edge. As we show in the supplemental material via numerical modeling of the system in a

180 coupled-mode tight-binding approximation, these nodal patterns persist for larger systems, with

181 the only difference being an emerging modulation of the peak heights and spacings across the edge.

182 An explicit construction of the edge states at maximal strain, also given in the supplemental

183 material, reveals that these edge states indeed approach the bound-state sequence of a harmonic

184 oscillator, with the corresponding sequences on the A and B sublattices offset by one pseudo-

185 Landau level.

186

We now explain how these offset nodal patterns reveal the underlying supersymmetry of the pseudo-Landau levels. This is encoded in the low-energy theory of the system, which is formulated as a continuum approximation for energies close to the central frequency ω_0. Relative to this central frequency, the pseudo-Landau levels are then described by an effective Hamiltonian[23,26,30]

$$H_0 = \begin{pmatrix} 0 & \pi^\dagger \\ \pi & 0 \end{pmatrix}. \tag{5}$$

where the Landau-level annihilation and creation operators π and $\pi^\dagger$ fulfill $[\pi, \pi^\dagger] = 2v^2\beta/a_0^2$ (we assume $\beta > 0$; for opposite deformation the operators π and $\pi^\dagger$ interchange their roles and become creation and annihilation operators). This corresponds to the Hamiltonian of a relativistic electron in a magnetic field, which is formally identical to a supersymmetric harmonic oscillator[23,31]. The link to the offset nodal patterns along the edges arises from the fact that $H_0^2 = \text{diag}(\pi^\dagger\pi, \pi\pi^\dagger)$ factorizes into two equidistant level sequences $E_n^2 = 2v^2 n\beta/a_0^2$ on the two sublattices, where $n = 0,1,2,3,...$ on the A sublattice, while on the B sublattice $n = 1,2,3,...$, so that the sequence is indeed offset by one. At the edge of the system, the creation operator $\pi^\dagger$ that connects these level sequences increases the number of nodes with each application by exactly one, so that the number of nodes coincides with the position of the level within the given symmetry sector of the theory. As mentioned above, this picture is further supported beyond the low-energy theory by the explicit construction of edge states given in the supplemental material. The experimentally observed offsets in the level sequence and the nodal patterns therefore both arise from a common origin.

Discussion

We achieved the direct observation of the formation of pseudo-Landau levels in deformed honeycomb systems, both spectrally as well as in terms of their key spatial features. In particular, adopting a flexible dielectric-resonator array design with a purposefully selected geometry allowed us to follow the formation of these levels in the transition from vanishing to large pseudomagnetic field strengths. In this way, we could observe how the 0th pseudo-Landau level originates from

the transformation of zigzag edge states into bulk states, whilst maintaining its characteristic anomalous polarization on only one of the two sublattices in the system. Extending these considerations to the higher-order levels allowed us to reveal a characteristic nodal structure of the pseudo-Landau level sequence that reflects the supersymmetric structure of the underlying low-energy description. These features underline the general usefulness to account for anomalous expectation values to provide a more general perspective on topological states.

Resolving the reported features in an experiment poses a significant challenge. In electronic systems such as graphene, spectral imaging techniques do not provide the required atomistic resolution, so that the information can only be extracted indirectly, for example from the Fourier transformation of form factors[32,33]. A better resolution is offered by photonic systems[17], which however so far could not access the characteristic spatial features of the pseudo-Landau levels in the bulk of the system, and furthermore considered a geometry that does not enable to observed fully formed flat-band pseudo-Landau levels[28]. Drawing on an acoustic analogue[34], a recent experiment[18] managed to excite a compacton-like state in the 0th Landau level, demonstrating its characteristic sublattice polarization in the bulk[26]. Here, we exploited an adaptable dielectric microwave-resonator array geometry to provide a complete characterization of the system from the unstrained to the fully strained case. This allows us to reveal how zigzag edge states transform into the bulk states of the anomalous 0th pseudo-Landau level, where they retain their characteristic sublattice polarization. Furthermore, this perspective dictates a natural geometry in which maximal pseudomagnetic fields can be attained, and for which the pseudo-Landau levels remain compatible with the boundary conditions at all field strengths, in contrast to the previous experiments. This is required to obtain pseudo-Landau levels that are flat, which we evidence spectrally by the observation of sharp peaks in the photonic density of states, and enables to reveal the supersymmetric signatures in the nodal structure.

Our results extend to a wide variety of flat-band systems, such as the rich physics arising from higher-order resonator modes in deformed honeycomb lattices, as reported for exciton polaritons in ref. 35. Practically, the observed spatial features should help to pave the way to applications such as flat-band lasers[13,26,36], as well as sublattice-dependent sensors where one could exploit that chiral-symmetry breaking perturbations equip the 0th Landau level with a finite weight on the

247   opposite sublattice.

248

249   **Materials and methods**

250

251   **A. Experiment**

252

253   The experimental setup is designed to realize a microwave system that is well approximated by a

254   nearest-neighbour tight-binding description[25]. The sites of the lattice are occupied by dielectric

255   microwave resonators with a cylindrical shape and made of ZrSnTiO ceramics (Temex-Ceramics,

256   E2000 series: 5 mm height, 8 mm diameter and a refractive index $n \approx 6$) sandwiched between

257   two metallic plates at a distance $h = 16$ mm. Each resonator supports a fundamental TE mode of

258   bare frequency $\omega_0 = 6.653$ GHz, which corresponds to the on-site energy of atoms in a tight-

259   binding model. Due to ohmic losses in the dielectric material and the metal, the quality factor of

260   this mode is $Q \simeq 6000$, leading to a resonance width $\Gamma \simeq 5$ MHz. As the resonance frequency is

261   below the cut-off frequency of the first TE mode defined by the two plates the adjacent resonators

262   are coupled through evanescent wave components leading to an approximately exponential decay

263   of the coupling strength t with the distance between the resonators[25]. The system is excited via a

264   loop antenna fixed in the movable top plate thus allowing to scan spatially the magnetic field B_z,

265   which is the only magnetic field component for this mode[37]. From the reflection measurements

266   performed by a vector network analyzer (ZVA 24 from Rohde & Schwarz) the local density of

267   states can be extracted (for details see ref. 25) and finally, by integrating over space, the density of

268   states. In all these experiments, we face an intrinsic on-site disorder of $\sim 0.15\%$ in the values of

269   ω_0.

270

271   **B. Modelling**

272

273   For the design of the system, we modelled finite strained photonic honeycomb lattices with a range

274   of system sizes and boundary geometries within coupled-mode tight-binding theory, in which we

275   accounted for the fundamental TE mode and incorporated the experimental distance dependence

276   of the coupling strengths following[25]. Exact diagonalization gives us access to the resonant modes

277   and their spatial intensity distribution. The modelling confirmed that the triaxial coupling profile

278 (1) can be attained by suitable positioning of the resonators, resulting in an excellent match with
279 the continuum theory predictions for the lowest Landau levels in systems as used in the
280 experiments. The modelling further confirmed that only for zigzag boundaries one can attain the
281 full sublattice polarization of the zeroth Landau level, and only for a triangular shape the Landau
282 levels become maximally degenerate.

283

290

291 **Author contributions**

292

293 MB and FM carried out the experiments and analyzed the data with input from UK. CP modelled
294 the system with input from HS, who provided the theory and initiated the project. All authors
295 contributed substantially to this work, including the interpretation of the results and the preparation
296 of the manuscript.

297

298 **Conflict of interest**
299 The authors declare that they have no conflict of interest.

300

301 **References:**

302

303 1. Hasan, M. Z. & Kane, C. L. Colloquium: Topological insulators. *Rev. Mod. Phys.* **82**,
304   3045-3067 (2010).
305 2. Benalcazar, W. A., Bernevig, B. A. & Hughes, T. L. Quantized electric multipole insulators.
306   *Science* **357**, 61-66 (2017)
307 3. Nielsen, H. B. & Ninomiya, M. The Adler-Bell-Jackiw anomaly and Weyl fermions in a
308   crystal. *Phys. Lett. B* **130**, 389-396 (1983).

4. Callan, C. G. & Harvey, J. A. Anomalies and fermion zero modes on strings and domain walls. *Nucl. Phys. B* **250**, 427-436 (1985).

5. Poli, C., Bellec, M., Kuhl, U., Mortessagne, F. & Schomerus, H. Selective enhancement of topologically induced interface states in a dielectric resonator chain. *Nature Commun.* **6**, 6710, (2015).

6. St-Jean, P. et al. Lasing in topological edge states of a one-dimensional lattice. *Nature Photon.* **11**, 651-656 (2017).

7. Zhao, H. et al. Topological hybrid silicon microlasers. *Nature Commun.* **9**, 981 (2018).

8. Parto, M. et al. Edge-mode lasing in 1d topological active arrays. *Phys. Rev. Lett.* **120**, 113901 (2018).

9. Reisner, M. et al. Self-shielded topological receiver protectors (2019). arXiv:1910.04684.

10. Guzmán-Silva, D. et al. Experimental observation of bulk and edge transport in photonic Lieb lattices. *New J. Phys.* **16**, 063061 (2014).

11. Mukherjee, S. et al. Observation of a localized at-band state in a photonic Lieb lattice. *Phys. Rev. Lett.* **114**, 245504 (2015).

12. Diebel, F., Leykam, D., Kroesen, S., Denz, C. & Desyatnikov, A. S. Conical diffraction and composite Lieb bosons in photonic lattices. *Phys. Rev. Lett.* **116**, 183902 (2016).

13. Poli, C., Schomerus, H., Bellec, M., Kuhl, U. & Mortessagne, F. Partial chiral symmetry breaking as a route to spectrally isolated topological defect states in two-dimensional artificial materials. *2D Materials* **4**, 025008 (2017).

14. Baboux, F. et al. Bosonic condensation and disorder-induced localization in a flat band. *Phys. Rev. Lett.* **116**, 066402 (2016).

15. Levy, N. et al. Strain-induced pseudo-magnetic fields greater than 300 Tesla in graphene nanobubbles. *Science* **329**, 544-547 (2010).

16. Gomes, K. K., Mar, W., Ko, W., Guinea, F. & Manoharan, H. C. Designer Dirac fermions and topological phases in molecular graphene. *Nature* **483**, 306 (2012).

17. Rechtsman, M. C. et al. Strain-induced pseudomagnetic field and photonic Landau levels in dielectric structures. *Nature Photon.* **7**, 153 (2013).

18. Wen, X. et al. Acoustic Landau quantization and quantum-hall-like edge states. *Nature Phys.* **15**, 352 (2019).

19. Guinea, F., Katsnelson, M. I. & Geim, A. K. Energy gaps and a zero-field quantum Hall

effect in graphene by strain engineering. *Nature Phys.* **6**, 30 (2010).

20. Fujita, M., Wakabayashi, K., Nakada, K. & Kusakabe, K. Peculiar localized state at zigzag graphite edge. *J. Phys. Soc. Jpn.* **65**, 1920 (1996).

21. Salerno, G., Ozawa, T., Price, H. M. & Carusotto, I. Propagating edge states in strained honeycomb lattices. *Phys. Rev. B* **95**, 245418 (2017).

22. Kunst, F. K., van Miert, G. & Bergholtz, E. J. Lattice models with exactly solvable topological hinge and corner states. *Phys. Rev. B* **97**, 241405 (2018).

23. Jackiw, R. Fractional charge and zero modes for planar systems in a magnetic field. *Phys. Rev. D* **29**, 2375-2377 (1984).

24. Bellec, M., Kuhl, U., Montambaux, G. & Mortessagne, F. Topological transition of Dirac points in a microwave experiment. *Phys. Rev. Lett.* **110**, 033902 (2013).

25. Bellec, M., Kuhl, U., Montambaux, G. & Mortessagne, F. Tight-binding couplings in microwave artificial graphene. *Phys. Rev. B* **88**, 115437 (2013).

26. Schomerus, H. & Halpern, N. Y. Parity anomaly and Landau-level lasing in strained photonic honeycomb lattices. *Phys. Rev. Lett.* **110**, 013903 (2013).

27. Sutherland, B. Localization of electronic wave functions due to local topology. *Phys. Rev. B* **34**, 5208-5211 (1986).

28. Poli, C., Arkinstall, J. & Schomerus, H. Degeneracy doubling and sublattice polarization in strain-induced pseudo-Landau levels. *Phys. Rev. B* **90**, 155418 (2014).

29. Rachel, S., Göthel, I., Arovas, D. P. & Vojta, M. Strain-induced Landau levels in arbitrary dimensions with an exact spectrum. *Phys. Rev. Lett.* **117**, 266801 (2016).

30. Castro Neto, A. H., Guinea, F., Peres, N. M. R., Novoselov, K. S. & Geim, A. K. The electronic properties of graphene. *Rev. Mod. Phys.* **81**, 109 (2009).

31. Thaller, B. The Dirac Equation (Springer Science & Business Media, New York, 2013).

32. Daimon, H., Imada, S., Nishimoto, H. & Suga, S. Structure factor in photoemission from valence band. *J. Electron Spectrosc.* **76**, 487-492 (1995).

33. Bostwick, A., Ohta, T., Seyller, T., Horn, K. & Rotenberg, E. Quasiparticle dynamics in graphene. *Nature Phys.* **3**, 36-40 (2006).

34. Abbaszadeh, H., Souslov, A., Paulose, J., Schomerus, H. & Vitelli, V. Sonic Landau levels and synthetic gauge fields in mechanical metamaterials. *Phys. Rev. Lett.* **119**, 195502 (2017).

35. Jamadi, O. et al. Direct observation of photonic Landau levels and helical edge states in strained honeycomb lattices (2020). Submitted.

36. Smirnova, D. A., Padmanabhan, P. & Leykam, D. Parity anomaly laser. *Opt. Lett.* **44**, 1120-1123 (2019).

37. Reisner, M., Mortessagne, F., Makri, E., Kottos, T. & Kuhl, U. Microwave limiters implemented by coupled dielectric resonators based on a topological defect mode and CT-symmetry breaking (2019). arXiv:1910.09203.

379 **Figure captions.**

380 **FIG 1**

381
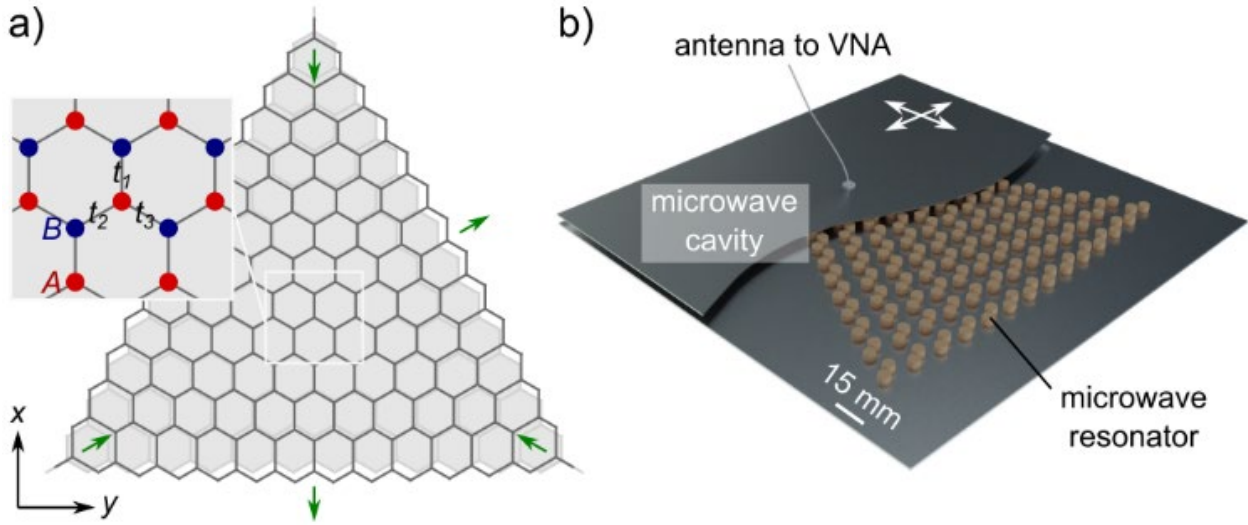
382
383
384

385 **Figure. 1 Experimental set-up. a** Sketch of the unstrained (gray) and strained (black) honeycomb
386 lattice geometry, forming a zigzag terminated triangle of size $L = 14$. The green arrows indicates
387 the directions ρ_l, $l = 1,2,3$, of the effective triaxial strain. Inset: the underlying lattice is
388 composed of two sublattices A (red) and B (blue). The local coupling strengths are denoted t_l.
389 They depend on the location of the bonds in the lattice [see Eq. (1) and the text for details). **b**
390 Illustration of the experimental set-up. The lattice is composed of 196 identically designed
391 cylindrical dielectric resonators that are coupled through the evanescent field of the fundamental
392 TE mode. The structure is placed inside a microwave cavity made of two metallic plates (top plate
393 only partially shown). A loop antenna, mounted on a scanning system (white arrows) crossing the
394 top plate and connected to a vectorial network analyzer (VNA), is used to generate and collect the
395 microwave signal both spectrally and spatially resolved, which allows to obtain the local density
396 of states in the system.

397

398 **FIG 2**
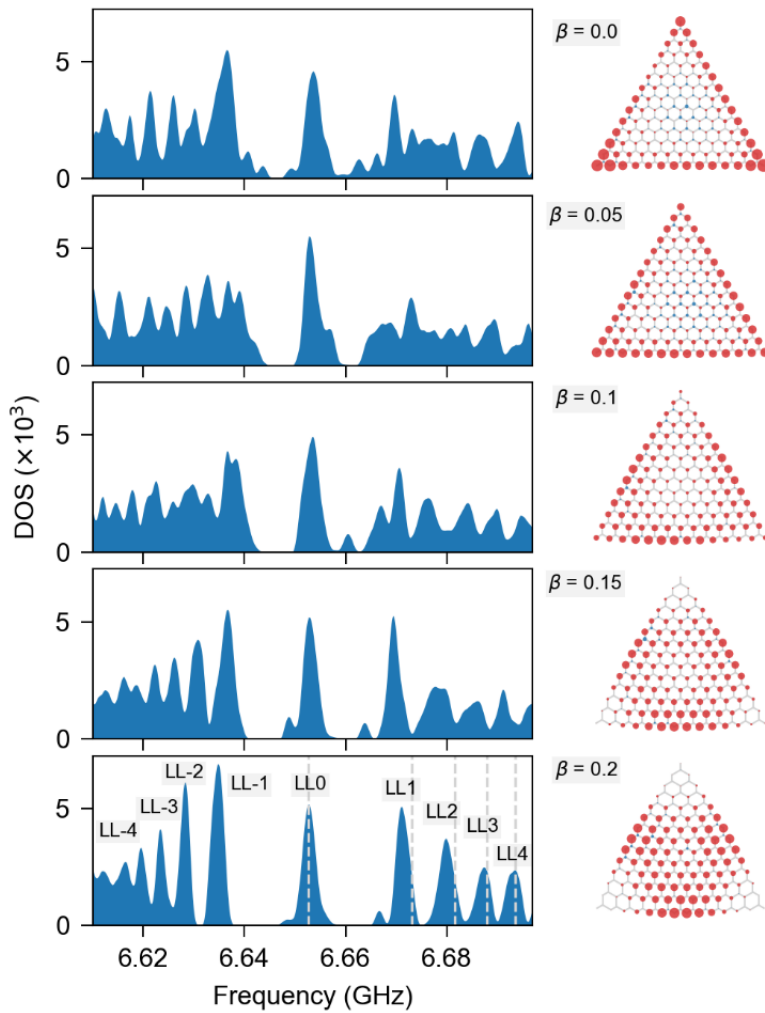
399

400

401 **Figure 2. Landau-level formation.** Experimentally determined density of states (left panels) and
402 spatially resolved mode intensity associated with the central peak centered at $\omega_0 = 6.653$ GHz
403 (right panels, obtained by integrating the local density of states over the peak). The area of the
404 circles corresponds to the intensity on the A sites (red) and B sites (blue). From top to bottom, the
405 pseudomagnetic field strength β varies from 0 to 0.2. The gray dashed lines in the total density of
406 states for $\beta = 0.2$ depict the expected pseudo-Landau levels frequencies from coupled-mode
407 theory. The formation of the 0th pseudo-Landau level proceeds continuously by transforming
408 zigzag edge states into bulk states, whilst retaining the degeneracy (spectral weight) and sublattice
409 polarization (remaining confined on the A sublattice).

410

411   **FIG 3**

412
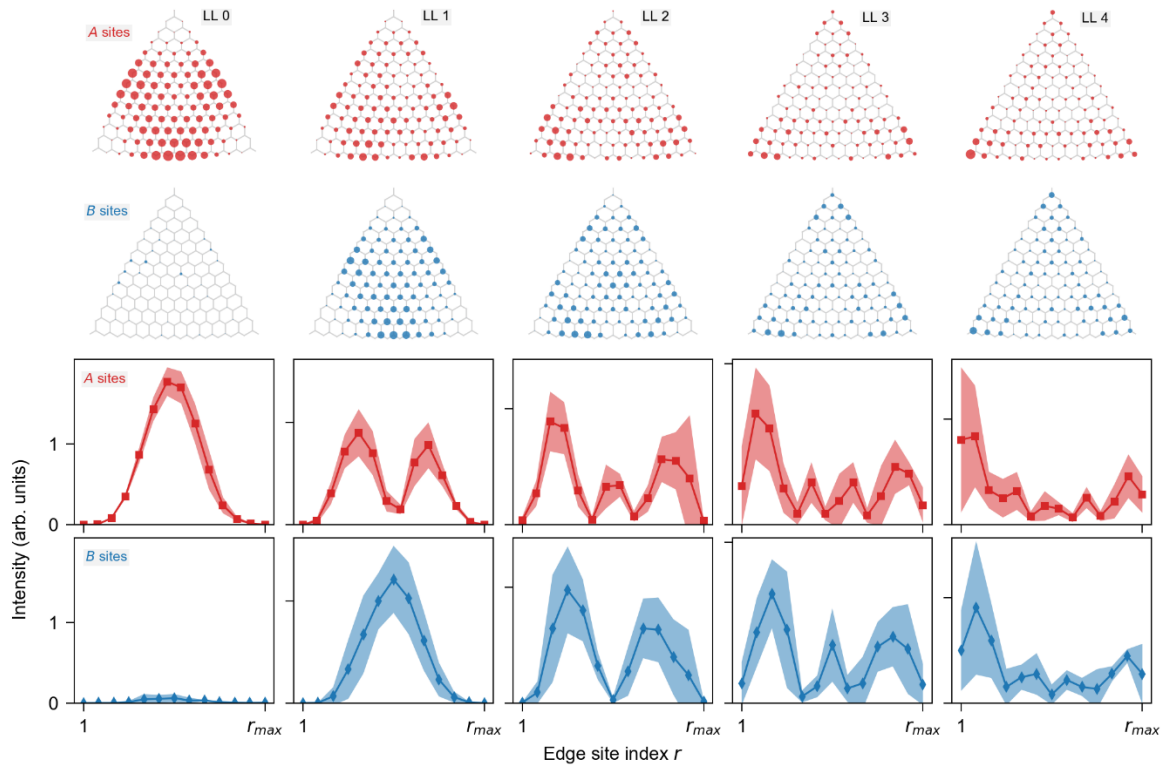
413

414

415   **Figure 3. Supersymmetric node structure.** Experimentally determined spatially resolved mode
416   intensities associated with the pseudo-Landau levels of index $n = 0$ to 4 (from left to right) for a
417   large pseudomagnetic field strength $\beta = 0.2$. Top rows: the area of the circles correspond to the
418   intensity on the A sites (above) and B sites (below). The 0th level is almost entirely localized on
419   the A sublattice, while all other levels have almost-equal overall weight on both sublattices.
420   Bottom rows: intensity on A sites (above) and B sites (below), averaged along the three extreme
421   edges at resonator position r. Note that $r_{\max} = 14$ (resp. 13) for A (resp. B) sites. For the higher-
422   order levels, the average is performed combining the indices $\pm n$. The shaded area corresponds to
423   the standard deviation. The two y-axis ticks indicated intensity values of 0 and 1 in arbitrary, but
424   uniformly applied units. The pseudo-Landau levels display a clear nodal structure offset by 1 mode
425   index, as further discussed in the text.

426